2010 IEEE International Conference on Robotics and Automation
Anchorage Convention District
May 3-8, 2010, Anchorage, Alaska, USA

Development and Preliminary Evaluation of an Actuated MRI-Compatible Robotic Device for MRI-Guided Prostate Intervention

Axel Krieger, Iulian Iordachita, Sang-Eun Song, Nathan B. Cho, Peter Guion, Gabor Fichtinger, Louis L. Whitcomb

Abstract— **This paper reports the design, development, and magnetic resonance imaging (MRI) compatibility evaluation of an actuated transrectal prostate robot for MRI-guided intervention. The robot employs an actuated needle guide with the goal of reducing interventional procedure times and increasing needle placement accuracy. The design of the robot, employing piezo-ceramic-motor actuated needle guide positioning and manual needle insertion, is reported. Results of a MRI compatibility study show no reduction of MRI image signal-to-noise-ratio (SNR) with the motors disabled and a 40% to 60% reduction in SNR with the motors enabled. The addition of radio-frequency (RF) shielding is shown to significantly reduce image SNR degradation due to the presence of the robotic device.**

I. Introduction

This paper reports the design, development, and magnetic resonance imaging (MRI) compatibility evaluation of an actuated robot for MRI-guided transrectal prostate intervention. The robot performs actuated needle alignment with the goal of reducing interventional procedure times and increasing needle placement accuracy. The robot employs piezo-ceramic-motor actuated needle guide positioning and manual needle insertion. This Section reviews the need for MRI-guided prostate intervention, Section II reports the robot design, Section III reports the results of an MRI compatibility study, and Section IV summarizes the results of this study.

A. Prostate Cancer Diagnosis and Therapy

Prostate cancer is the most common cancer in men in the United States. In 2009, an estimated 192,280 men will be diagnosed with prostate cancer and 27,360 will die of this disease [16]. Each year approximately 1.5 million prostate biopsy procedures are performed. Recent projections by the American Cancer Society predict that in 2015 there will be over 450,000 new cases of prostate cancer diagnosed each year, more than doubling the current incidence. This section briefly reviews the current state-of-the-art in prostate cancer diagnosis and therapy. The two commonly used methods for screening men for prostate cancer are the prostate-specific antigen (PSA) blood test and the digital rectal exam (DRE). The American Cancer Society recommends screening men, beginning at age 50, yearly with PSA test and DRE.

Ultrasound-Guided Prostate Intervention: The definitive diagnosis for prostate cancer is core needle biopsy pursuant to either an elevated PSA level or a positive DRE. The "Gold Standard" of guiding biopsy, as well as of most local therapies, is transrectal ultrasound (TRUS) [26]. The physician manually places a TRUS probe in the rectum of the patient and, under ultrasound guidance, inserts a biopsy needle through the wall of the rectum into the prostate gland. The needle removes a half-cylinder of tissue, which is examined pathologically to determine if cancer is present. Several biopsy samples are taken from different areas of the prostate. Usually six (hence "sextant biopsy") to eighteen cores are removed from upper, mid, and lower areas of the left and right sides to obtain a representative sample of the gland and determine the degree and extent of cancer.

TRUS-guided prostate biopsy is widely employed due to its real-time nature, relative low cost, and ease of use. The limitations of this and other current prostate biopsy methods, however, are substantial. Using standard techniques, biopsy of men with PSA values in the range of 4-10 ng/ml generally result in a detection rate of 20% -30% [29], [36]. Numerous studies have shown that TRUS-guided prostate biopsy fails to detect cancer in at least 20% of patients with cancer [24], [28], [37]. Other studies report that TRUS biopsies are limited by low sensitivity of 60% with only 25% positive predictive value [17], [35]. As a consequence, in more than 20% of cancers, at least two biopsy sessions are required to diagnose the tumor — which mounts to more than 200,000 repeat biopsy cases annually in the United States. Despite rapid advances in ultrasound imaging methods, TRUS imaging is generally unable to differentiate between healthy tissue and lesions in the prostate. In consequence, contemporary TRUS-guided biopsy can not identify or target lesions, but rather samples six or more representative locations in the gland. Studies of the efficacy of 6 versus 12 biopsy samples showed no significant difference in cancer detection [23], [25]. This suggests that increase in the number of samples does not solve the problem of prostate cancer detection, and it suggests that improved biopsy targeting promises to be advantageous.

Iulian Iordachita, Sang-Eun Song, Nathan B. Cho, and Louis L. Whitcomb are with the Laboratory for Computational Sensing and Robotics (LCSR) and Department of Mechanical Engineering (ME), Johns Hopkins University (JHU), Baltimore, Maryland, USA. Axel Krieger was with JHU LCSR and ME, and is presently with Sentinelle Medical Inc., Toronto, Canada. Gabor Fichtinger is with the School of Computing, Queen's University, Kingston, Ontario, Canada. Peter Guion is with the Radiation Oncology Branch, National Cancer Institute, National Institutes of Health, Bethesda, Maryland, USA.

This study was supported in part by the National Science Foundation (NSF) under Grant ERC9731478 and in part by the National Institutes of Health (NIH) under Grant RO1-EB02963.

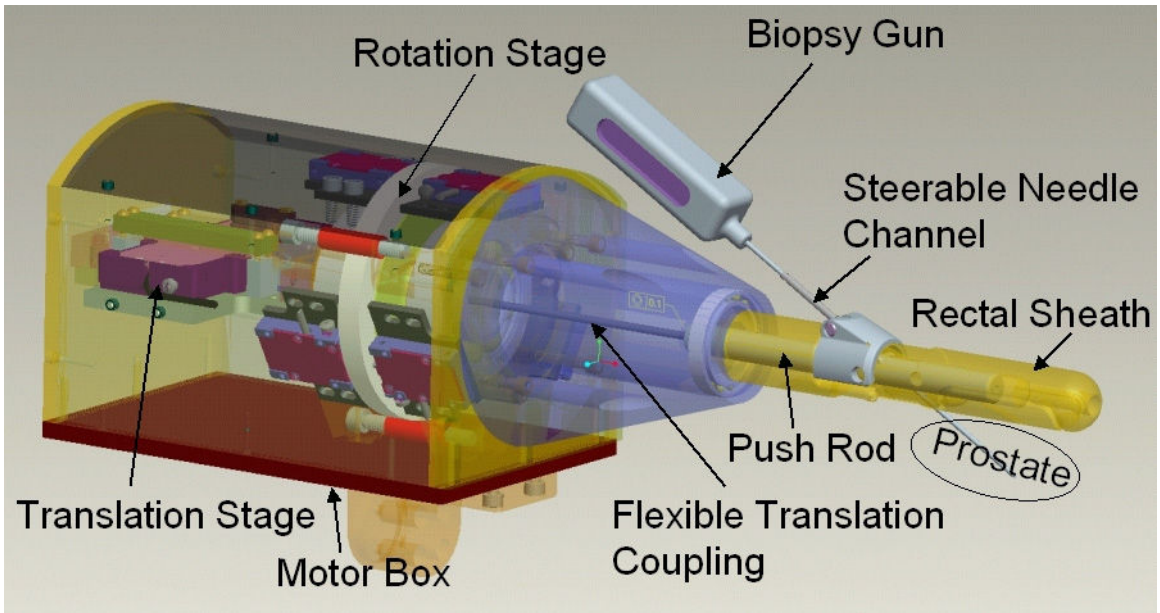

Fig. 1. CAD drawing of the actuated robot for prostate intervention, consisting of steerable needle channel, rectal sheath, push rod, rotation stage, translation stage, flexible translation coupling, and motor box. Biopsy gun and outline of prostate are shown, indicating prone positioning in a transrectal prostate biopsy procedure.

B. The Case for MRI-Guided Prostate Intervention

MRI possesses many of the capabilities that TRUS is lacking. MRI is an attractive choice for image-guidance, primarily due to its high sensitivity for detecting prostate tumors [37], [39], high spatial resolution, excellent soft tissue contrast, and multiplanar volumetric imaging capabilities.

Recent advances with phased array pelvic and endorectal coils have dramatically enhanced the ability of MRI to visualize prostate tissues [2], [27]. MRI can clearly visualize the prostate and its substructure including the peripheral zone (PZ). As the PZ is the most common site of origin of prostate cancer, localizing and targeting PZ suspicious lesions during prostate biopsy may increase cancer detection rate. T2 weighted images can identify suspicious nodules in the prostate, allowing targeted biopsy and local therapy.

Several novel MRI imaging methods are currently being developed in an effort to improve the specificity of prostate cancer detection and characterization. Novel MRI imaging methods include MRI spectroscopy [22], [37], dynamic contrast enhancement MRI, T2 maps, and line-scan diffusion tensor imaging [4], [38]. MRI can also visualize the distribution and buildup of injected liquid agents in the prostate [7], [33], and solid capsules [8], [33]. MRI can monitor the progress of thermal therapies in real-time [5], [15].

In summary, MRI provides a promising image guidance modality for prostate interventions. There is also an urgent clinical need to investigate diagnostic capabilities of emerging MRI imaging techniques. MRI could potentially overcome the shortcomings of ultrasound as the image guidance modality for the diagnosis and local therapy for prostate cancer.

C. Previously Reported MRI-Compatible Prostate Intervention Systems

This section reviews MRI-compatible systems for prostate intervention utilizing transrectal, transperineal, and transgluteal approach.

1) Transrectal Approach: In [7], [19]–[21], [32], [33] the authors reported the development and clinical evaluation of two generations of MRI-guided system for transrectal prostate biopsies, therapy injection, and marker placements. The system, called the APT-MRI, contains a single-loop MRI endorectal imaging coil and employs active or passive tracking for device localization. In vivo and in vitro accuracy results were reported. This clinical prototype has been successfully used in over 40 patient procedures to date. In [3] Beyersdorff and in [12] Engelhard report MRI-guided transrectal needle biopsies in clinical studies with a system (Invivo Germany GmbH, Schwerin, Germany) employing manual alignment of a needle sleeve. Elhawary reported a prototype robotic system using linear piezo-ceramic motors for transrectal prostate biopsy [11].

2) Transperineal Approach: MRI-guided transperineal prostate intervention has been demonstrated in clinical studies inside an open MRI scanner [9] and conventional closed MRI scanner [31]. The surgical assistant robot reported by Chinzei [6] was adapted to assist transperineal intraprostatic needle placement [10]. Tadakuma reported the use of dielectric elastomer actuators (DEAs) in a pre-clinical prototype MRI compatible robot for transperineal needle placement in the prostate [34]. Stoianovici reported pre-clinical phantom experiments with a pneumatically actuated device for tranperineal brachytherapy seed placement [30]. In [13] Fischer reported phantom experiments with a pneumatically actuated robot with manual needle insertion. Goldenberg

reported phantom targeting and MRI compatibility tests for a robotic system employing ultrasonic actuators for closed MRI scanners [14].

3) Transgluteal Approach: Zangos reported preliminary clinical results with 25 patients using the transgluteal approach with an open configuration 0.2T MRI scanner [40], with targeting based on prior diagnostic images acquired with higher field strength MRI. In [41] Zangos reported usage of the Innomotion pneumatic robot in a cadaver study at 1.5T for transgluteal prostate needle placements.

D. The Need for an Actuated Transrectal MRI-Compatible Prostate Intervention System

Existing MRI compatible manual biopsy needles and guns are too large to be employed while the patient is within the confined space of the MRI scanner bore. Hence, present day MRI-guided biopsy procedures are performed with the patient outside the scanner bore. Accordingly, all previously reported clinical MRI compatible prostate intervention systems require the patient to be removed from the MRI scanner during the interventional procedure – e.g. needle insertion, biopsy, or gold marker placement. A fully actuated robot could enable both imaging and interventional procedures to be performed entirely inside the MRI scanner, without removing the patient from the MRI scanner for interventional procedures. Moreover, a fully actuated robot could simplify and speed up the interventional procedure; allow for real-time visualization of the needle insertion; enable detection of prostate deformation, misalignment, and deflection of the needle; and allow for on-the-spot corrections to needle placements.

II. Robot Design

This Section reports the design of a novel robot, for transrectal prostate intervention with actuated needle alignment and manual needle insertion. Combining actuated needle alignment with manual needle insertion provides a much quicker path to clinical trials and provides a significant step towards the goal of a fully actuated robot. Automating the degrees-of-freedom (DOF) for alignment of the needle might lead to a faster, easier, and more accurate interventional procedure, and might eliminate the learning curve necessary to operate the robot, while maintaining direct physician control for needle insertion.

Figure 1 shows a CAD drawing of the actuated prostate robot. The robot employs similar manipulator mechanics to the APT-MRI system reported in [19], [21]. The robot employs the same three DOF in rotation of the rectal sheath, needle angle change, and needle insertion. The robot uses the same rectal sheath, steerable needle channel, and push rod. The robot provides actuated rotation and needle angle change for needle positioning. Needle insertion is performed manually.

The robot consists of a rotation stage and a translation stage with flexible coupling, integrated in a motor box. Non-magnetic piezo-ceramic motors from the HR series piezo-electric motors (Nanomotion Inc., Yokneam, Israel) were selected for actuation. Motors are placed 20 cm or more away from the prostate to eliminate susceptibility artifacts on the MRI images, caused by metallic motor components.

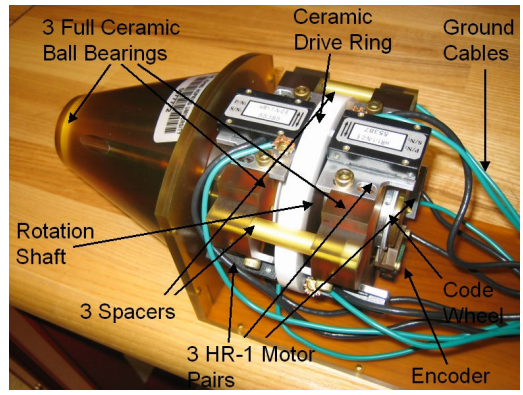

Fig. 2. Photograph of the rotation stage for the actuated robot. Three pairs of HR-1 Nanomotion motors rotate a ceramic ring placed on the rotation shaft.

Nanomotion non-magnetic HR motors consist of one, two, four, or eight linear piezo-ceramic elements stacked inside an aluminum enclosure. Each element provides a dynamic stall force of 4 N and exerts a pre-load of 18 N. The pre-load is applied constantly and provides high break forces when the motors are powered off. Maximum velocity for all HR series motors is 250 mm/sec.

A. Rotation Stage

Figure 2 shows a photograph of the rotation stage for the robot. Nanomotion motors can be mounted either radially or axially to exert rotation of a ceramic drive ring. The rotation axis for performing transrectal biopsy intervention is closely aligned with the main axis of the MRI scanner bore. Radial space is limited in an MRI scanner bore, while axial space is ample. Hence, axial motor configuration was selected for the rotation stage. Single-element motors (HR-1 motors) were selected for the rotation stage, since HR-1 motors are best suited for axial configuration in combination with a small drive ring.

Each HR-1 motor exerts an axial pre-load of 18 N on the ceramic drive shaft. Aligning the HR-1 motors in opposing pairs limits the net force exerted on the ring and minimizes deflection and bearing loads of the rotation stage. Three pairs of HR-1 motors, with a combined dynamic stall force of 24 N for the six motors, provide a designed maximum torque of 1.08 Nm, when rotating a drive ring with center diameter of 90 mm. The combination of three pairs of HR-1 motors, spaced evenly in 120 degrees increments along the circumference of a 90-mm-diameter drive ring, meets the torque requirements and was selected for the robot. Full ceramic ball bearings (VXB.com Ball Bearings, Anaheim, CA) were selected for the rotation stage. Two angular contact bearings are placed on either side of the ceramic ring and are axially pre-loaded to eliminate play for optimal motor performance.

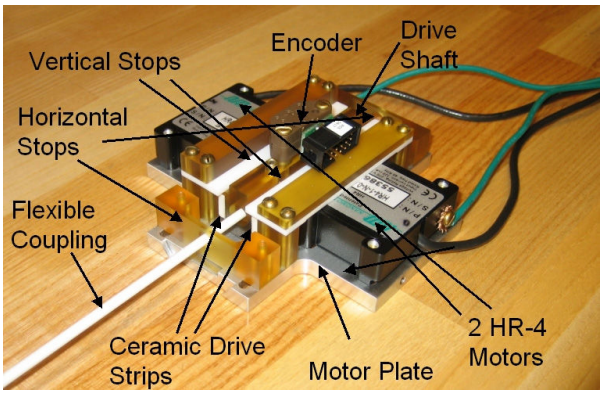

Fig. 3. Photograph of the translation stage for the actuated robot. A pair of HR-4 Nanomotion motors pushes on ceramic drive strips and provides linear motion of a drive shaft.

B. Translation Stage

Figure 3 shows a photograph of the translation stage for the actuated robot using two Nanomotion HR-4 motors with four motor elements each. Nanomotion motors are intended for usage in combination with high precision, low friction, crossed roller linear bearings for optimal motor performance. An MRI compatible implementation of crossed roller bearings is difficult to design and would be expensive. Mechanical evaluation of a piezo-electric motor and linear-bearing test assembly revealed that better motor performance can be achieved when linear bearings are eliminated, and side-to-side alignment of the drive shaft is set using only the fingers of opposing motors. This low-cost linear drive implementation was used for the translation stage of the actuated robot.

Opposing pairs of HR-4 Nanomotion motors are axially pre-loaded on ceramic drive strips and provide linear motion of a drive shaft that slides axially forward and backward on a motor plate. Side-to-side alignment of the drive shaft is set by the pre-load of the opposing ceramic motor fingers. The low-cost bearing implementation reduces dynamic stall force, reduces maximum speed, and creates an uneven velocity profile of the drive shaft over long travels. The linear travel necessary to change the needle angle the full range, from 17.5 degrees to 40 degrees, is 28.7 mm. Only device friction has to be overcome to change the needle angle and slow speeds are acceptable for actuating the needle angle change. The short travel, slow speed requirements, combined with closed-loop position control allow the usage of the HR-4 motors in combination with the low-cost bearing implementation.

C. Materials

The robot is constructed mostly of plastic materials, foremost of Ultem, selected for its structural stability, machinability, and low cost. Ball bearings and bearing races for the rotation stage are fully ceramic. Vertical stops and rotating parts of the flexible coupling for the translation stage are constructed of Teflon to reduce friction. All larger metallic components are placed inside the motor box, such as motors and motor plates. The motor plates for the rotation stage and translation stage are constructed of aluminum for increased stability and heat dissipation, in comparison to Ultem. The motor box is separated by 20 cm from the field-of-view (FOV) by the rotation shaft and rectal sheath to avoid creation of susceptibility artifacts on MRI images. The rectal sheath is built out of medical grade Ultem with small aluminum and brass parts for needle channel and axles.

D. Position Tracking

The robot uses the hybrid tacking method described in [19]. Initial device registration is performed using two Beekley markers (Beekley Inc., Bristol, CT) integrated into the rectal sheath and two markers placed concentrically to the needle channel. The initial position and orientation of the robot is computed after automatic segmentation of the markers on MRI images. The robot employs electro-optical encoding for the rotation and needle angle change DOF. Modular EM1 electro-optical encoders (US Digital, Vancouver, Washington), code wheel, and code strip were selected for joint encoding.

The advantage of fiber optic joint encoding, [19], over electro-optical joint encoding, is the inherent MRI safety and compatibility of fiber optics. No electrical signals or conductive materials are present to potentially cause RF heating and imaging artifacts, making fiber optics the safe choice for performing clinical trials. Advantages of electro-optical encoders include the ubiquitous availability of inexpensive commercial electro-optical encoders, high resolution and repeatability, and easy encoder signal integration into a controller. In contrast to the system reported in [19], the actuated robot already contains piezoelectric motors, which require power and ground connections. Adding cables for supplying the electro-optical encoders with power and conducting encoder signals does not significantly add to the complexity of the design or the safety risk.

Modular EM1 electro-optical encoders (US Digital, Vancouver, Washington), code wheel, and code strip were selected for joint encoding. The EM1 encoders are available in high resolution and feature a non-magnetic design with low metal content. A two inch diameter code wheel and EM1 encoder with 2500 cycles per revolution (CPR) was selected for encoding the rotation. The encoder supports quadrature encoding, so each cycle provides four different counts. The resulting resolution for rotation is $360\ degrees/10000\ counts = 0.036\ degrees/count$. A 500 lines per inch (LPI) EM1 encoder and code strip was selected for encoding translation of the drive shaft and indirectly encoding the needle angle change. The resulting resolution for encoding translation is $25.4\ mm/2000\ counts = 0.013\ mm/count$. The average resolution for encoding needle angle change can be calculated by dividing the angular travel by the translational travel and multiplying the result with the translational resolution. The calculated average needle angle resolution is thus $(40\ degrees - 17.5\ degrees)/28.7\ mm * 0.013\ mm/counts = 0.01\ degrees/count$. This resolution is an order of magnitude higher than for the fiber optical encoders of the system reported in [19], with 0.25

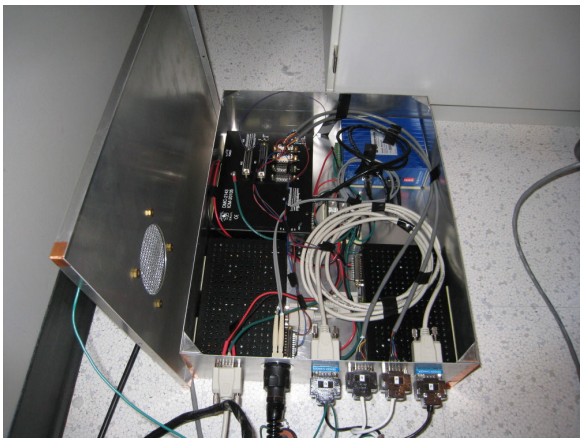

Fig. 4. Photograph of the controller box designed to be placed inside the scan room. The box contains motor amplifiers, motion controller, and media converter.

degrees/count resolution for rotation and 0.1 degrees/count resolution for change of needle angle.

E. Controller

The controller box contains two Nanomotion AB5 motor amplifiers, a DMC-21x3 Ethernet motion controller (Galil Motion Control, Rocklin, California), and a EIR-M-ST fiber optic to Ethernet media converter (B&B Electronics Mfg. Co., Ottawa, IL). The only electrical connection to the controller is a filtered 24 V DC power supply through the penetration panel. External communication is via fiber optic Ethernet. IP66/67 Harsh Environment Multimode Duplex LC Cable (L-com Inc., North Andover, MA) was selected for the fiber optical connection because of its rugged design. LC-to-ST converter cables are used to connect to the media converter. A second box (Figure 4, right) is placed outside the scanner room containing power supply and the EIR-M-ST media converter counterpart.

III. MRI-Compatibility Evaluation

Thus Section reports the results of a MRI compatibility study to determine the effects of the robot on signal-to-noise-ratio (SNR) of the MRI images. SNR is described by the signal intensity in the center of the homogeneous phantom divided by the noise intensity in the periphery, as defined by the National Electrical Manufacturers Association (NEMA) standard for determining SNR in MRI images [1]. Signal intensity is defined as the mean pixel intensity in the region of interest (ROI). Noise intensity is defined as the root mean square (RMS) signal intensity in an ROI outside of the phantom. All tests were performed on a 3T Philips Achieva MRI scanner (Philips Medical Systems, Best, NL). Three imaging sequences using the same imaging parameters were used for the compatibility study of the robot: T1 FFE, and T2 TFE. Each set of experiments consisted of the phantom being imaged alone (baseline) and subsequently imaged in the presence of each actuator in its power off configuration, power on configuration, and moving configuration. The receiving imaging coils used for the experiments were two-channel medium-size flex coils consisting of two panels. One panel was placed underneath the phantom, the other one on top of the phantom (Figure 5).

Three common MR sequences for diagnostic, real-time and functional imaging were selected to test the compatibility of the actuators (Table I): T1 weighted fast gradient echo (T1) and T2 weighted fast spin echo (T2) sequences for diagnostic imaging, fast gradient echo (TFE) sequence representing real-time imaging used for functional imaging.

The phantom was imaged under the following eleven configurations:

1) **Baseline:** Image the phantom with no robot or controller present in the scanner room.
2) **Off-US:** Image the phantom after placing the robot next to the phantom and the tranrectal probe on top of the phantom. The phantom and sheath position approximate prostate and sheath position in a clinical procedure. The controller is located in the scanner room and is connected, but is powered off.
3) **Off-SH:** As per (2), with additional shielding.
4) **Disabled-US:** Image the phantom after powering the controller on, but disabling the motor amplifiers.
5) **Disabled-SH:** As per (4), with additional shielding.
6) **Roll-US:** Image the phantom with the roll motor amplifier enabled, but the motor not moving.
7) **Roll-SH:** As per (6), with additional shielding.
8) **Pitch-US:** Image the phantom with the pitch (translation) motor amplifier enabled
9) **Pitch-SH:** As per (8), with additional shielding.
10) **Both-US:** Image the phantom with both roll and pitch (translation) motor amplifiers enabled.
11) **Both-SH:** As per (10), with additional shielding.

In configurations 2, 4, 6, 8, and 10 the body of the robot was unshielded. In configurations 3, 5, 7, 9, and 11 the body of the robot was covered with additional radio-frequency (RF) shielding (Z-3250-CN High Performance EMI Shielding Cloth, Zippertubing Co., Los Angeles, CA). Ten image slices were obtained of the phantom for each configuration for each image sequence and the SNR was calculated for each image slice. Figure 6 shows the SNR results, averaged for the 10 slices, for the three sequences. Figure 7 shows representative T2 weighted images of the spherical phantom under different configurations acquired during the MRI compatibility study.

The following are the most significant observations of the MRI compatibility study for the actuated robot:

1) The SNR exhibits modest spatial variation — measurements were uniform across the multiple slices of a single scan sequence.
2) The actuated robot does not cause any reduction in SNR in the motors-off configuration — thus enabling interleaved imaging and motion.
3) Turning the controller on with motors disabled reduces the SNR by 50% in without RF shielding, but SNR is only slightly degraded with RF shielding.
4) Turning the controller on with motors enabled reduces the SNR by 80% without RF shielding, but SNR is only reduced by 40% to 60% with RF shielding.

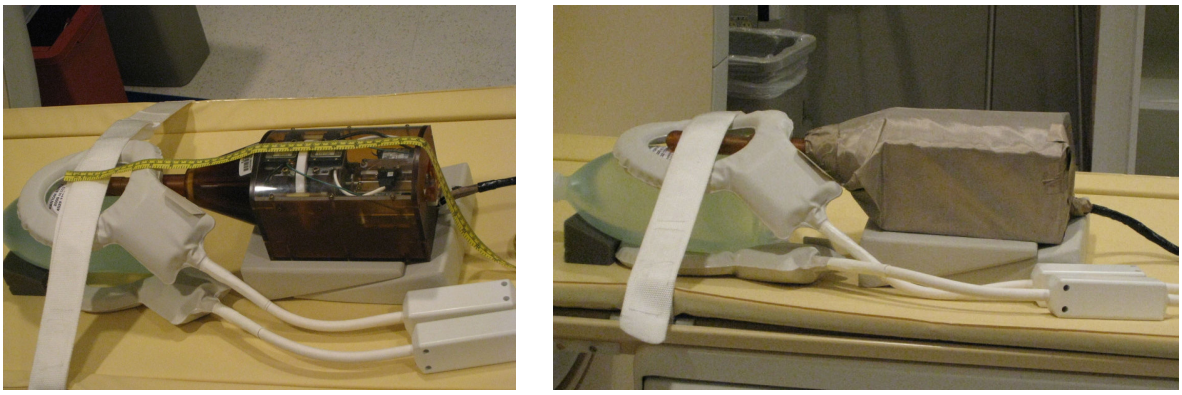

Fig. 5. Experimental setup for compatibility test in 3T MR scanner. Left image shows unshielded robot, phantom, and imaging coils. Right image shows shielded robot, phantom, and imaging coils.

Protocol	Slice Thick-ness (mm)	FOV (mm)	# of Slices (ms)	TE (ms)	TR	Flip Angle	NEX	Pixel Band-width Hz/pixel
T1	5	240	3	2.3	225.0	75°	1	1059.0
T2	5	240	3	90.0	3000.0	90°	1	1035.7
TFE	5	240	3	10.0	26.0	70°	1	1752.5

TABLE I

SCAN PARAMETERS FOR MOTOR COMPATIBILITY TRIAL.

5) Noise appears as vertical "zipper" streaks in the MR images — a well-known effect of RF interference.
6) All three sequences show similar SNR behavior.
7) The addition of RF shielding improves the SNR by a factor 200% to 500% in comparison to the same robot without RF shielding.

IV. CONCLUSION

This paper reported the design, development, and MRI compatibility evaluation of an actuated transrectal prostate robot for MRI-guided intervention. The robot employs actuated needle alignment with the goal of reducing interventional procedure times and increasing needle placement accuracy. The current version of the robot employs actuated needle guide positioning and manual needle insertion. Piezoceramic motors were selected as actuators for the robot. The design of the rotational stage and translational stage of the robot were reported. The MRI compatibility of the robot was analyzed, showing no reduction of SNR in the motor off configuration and a 40 % to 60 % reduction in SNR with the motors on. The addition of RF shielding significantly improved image SNR quality.

Although beyond the scope of the present study, needle targeting accuracy studies have been performed with this new device. In a study of seven MRI-guided biopsy needle placements in a prostate phantom, average in-plane error for the biopsy needles was 2.4 mm with a maximum error of 3.7 mm [18].

ACKNOWLEDGEMENTS

We are grateful to Mr. Mike Franckowiak and Mr. Walter Krug for their expert machining of the actuated robot prototype.

REFERENCES

[1] *Determination of Signal-to-Noise Ratio (SNR) in Diagnostic Magnetic Resonance Imaging, NEMA Standard Publication MS 1-2008*. The Association of Electrical and Medical Imaging Equipment Manufacturers, 2008. `http://www.nema.org/stds/ms1.cfm`.

[2] S. Adusumilli and E. S. Pretorius. Magnetic resonance imaging of prostate cancer. *Seminars in Urologic Oncology*, 20(3):192–210, Aug 2002.

[3] D. Beyersdorff, A. Winkel, B. Hamm, S. Lenk, S. A. Loening, , and M. Taupitz. MR imaging-guided prostate biopsy with a closed MR unit at 1.5T: Initial results. *Radiology*, 234(2):576–581, February 2005.

[4] I. Chan, W. Wells, R. V. Mulkern, S. Haker, J. Zhang, K. H. Zou, S. E. Maier, and C. M. C. Tempany. Detection of prostate cancer by integration of line-scan diffusion, T2-mapping and T2-weighted magnetic resonance imaging; a multichannel statistical classifier. *Medical Physics*, 30(9):2390–2398, Sep 2003.

[5] J. C. Chen, J. A. Moriarty, J. A. Derbyshire, R. D. Peters, J. Trachtenberg, S. D. Bell, J. Doyle, R. Arrelano, G. A. Wright, R. M. Henkelman, R. S. Hinks, S. Y. Lok, A. Toi, and W. Kucharczyk. Prostate cancer: MR imaging and thermometry during microwave thermal ablation-initial experience. *Radiology*, 214(1):290–297, Jan 2000.

[6] K. Chinzei, N. Hata, F. A. Jolesz, and R. Kikinis. MRI compatible surgical assist robot: System integration and preliminary feasibility study. In *Medical Image Computing and Computer-Assisted Intervention (MICCAI)*, volume 1935, pages 921–930, October 2000.

[7] S. L. Chowning, R. C. Susil, A. Krieger, G. Fichtinger, L. L. Whitcomb, and E. Atalar. A preliminary analysis and model of prostate injection distributions. *Prostate*, 66(4):344–357, Mar 2006.

[8] A. V. D'Amico, R. Cormack, C. M. Tempany, S. Kumar, G. Topulos, H. M. Kooy, and C. N. Coleman. Real-time magnetic resonance image-guided interstitial brachytherapy in the treatment of select patients with clinically localized prostate cancer. *International Journal of Radiation Oncology Biology Physics*, 42(3):507–515, Oct 1998.

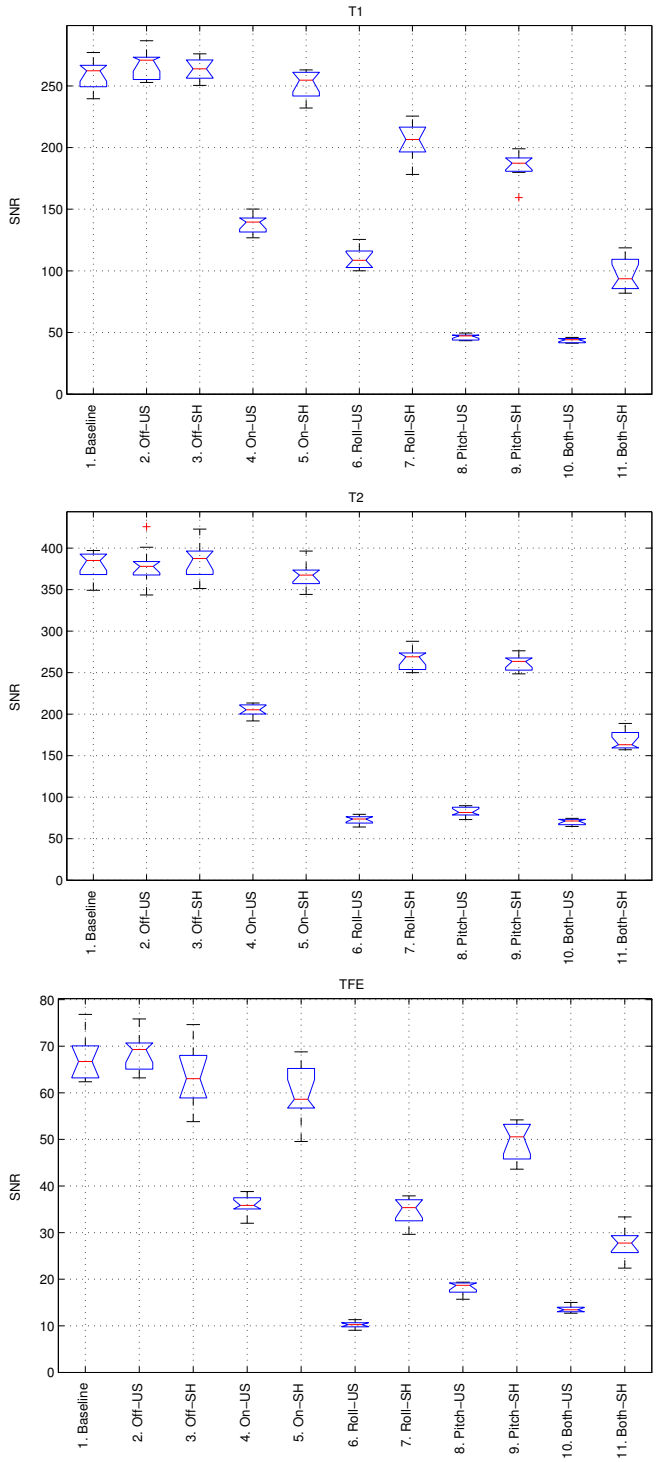

Fig. 6. SNR for T1 scans (top), T2 scans (middle), and TFE scans (bottom).

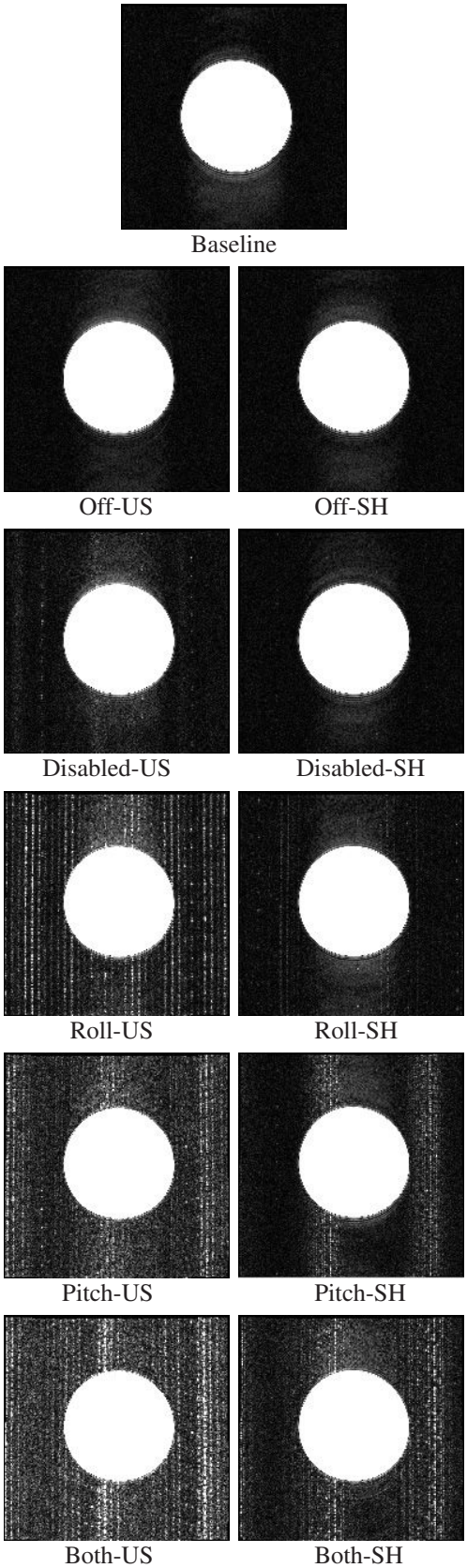

Fig. 7. Representative T2 phantom images showing (from top to bottom) baseline, Off, Disabled, Roll, Pitch, and Both. Left images are for the case of the unshielded robot. Right images are for the case of the shielded robot.

[9] A. V. D'Amico, C. M. Tempany, R. Cormack, N. Hata, M. Jinzaki, K. Tuncali, M. Weinstein, and J. P. Richie. Transperineal magnetic resonance image guided prostate biopsy. *Journal of Urology*, 164(2):385–387, Aug 2000.

[10] S. P. DiMaio, S. Pieper, K. Chinzei, N. Hata, S. J. Haker, D. F. Kacher, G. Fichtinger, C. M. Tempany, and R. Kikinis. Robot-assisted needle placement in open MRI: system architecture, integration and validation. *Comput Aided Surgery*, 12(1):15–24, Jan 2007.

[11] H. Elhawary, A. Zivanovic, M. Rea, B. Davies, C. Besant, D. McRobbie, N. de Souza, I. Young, and M. Lamprth. The feasibility of MR-image guided prostate biopsy using piezoceramic motors inside or near to the magnet isocentre. *International Conference on Medical Image Computing and Computer-Assisted Intervention*, 9(Pt 1):519–526, 2006.

[12] K. Engelhard, H. P. Hollenbach, B. Kiefer, A. Winkel, K. Goeb, and D. Engehausen. Prostate biopsy in the supine position in a standard 1.5-T scanner under real time MR-imaging control using a MR-compatible endorectal biopsy device. *European Radiology*, 16(6):1237–1243, Jun 2006.

[13] G. S. Fischer, I. Iordachita, C. Csoma, J. Tokuda, S. P. DiMaio, C. M. Tempany, N. Hata, and G. Fichtinger. MRI-compatible pneumatic robot for transperineal prostate needle placement. *IEEE/ASME Transactions on Mechatronics*, 13(3):295–305, June 2008.

[14] A. A. Goldenberg, J. Trachtenberg, W. Kucharczyk, Y. Yi, M. Haider, L. Ma, R. Weersink, and C. Raoufi. Robotic system for closed-bore MRI-guided prostatic interventions. *IEEE/ASME Transactions on Mechatronics*, 13(3):374–379, June 2008.

[15] S. J. Graham, G. J. Stanisz, A. Kecojevic, M. J. Bronskill, and R. M. Henkelman. Analysis of changes in MR properties of tissues after heat treatment. *Magnetic Resonance in Medicine*, 42(6):1061–1071, Dec 1999.

[16] A. Jemal, R. Siegel, E. Ward, Y. Hao, J. Xu, and M. J. Thun. Cancer Statistics, 2009. *CA: A Cancer Journal for Clinicians*, page caac.20006, 2009.

[17] D. W. Keetch, J. M. McMurtry, D. S. Smith, G. L. Andriole, and W. J. Catalona. Prostate specific antigen density versus prostate specific antigen slope as predictors of prostate cancer in men with initially negative prostatic biopsies. *Journal of Urology*, 156(2 Pt 1):428–431, Aug 1996.

[18] A. Krieger. *Advances in Magnetic Resonance Image Guided Robotic Intervention*. PhD thesis, Johns Hopkins University, 2008.

[19] A. Krieger, G. Metzger, G. Fichtinger, E. Atalar, and L. L. Whitcomb. A hybrid method for 6-DOF tracking of MRI-compatible robotic interventional devices. In *Proceedings - IEEE International Conference on Robotics and Automation*, volume 2006, pages 3844–3849, Orlando, FL, United States, May 2006.

[20] A. Krieger, R. Susil, A. Tanacs, G. Fichtinger, L. Whitcomb, and E. Atalar. A mri compatibledevice for MRI guided transrectal prostate biopsy. *International Society of MagneticResonance Imaging in Medicine, Tenth Scientific Meeting, Honolulu*, page 338, 2002.

[21] A. Krieger, R. C. Susil, C. Menard, J. A. Coleman, G. Fichtinger, E. Atalar, and L. L. Whitcomb. Design of a novel MRI compatible manipulator for image guided prostate interventions. *IEEE Transactions on Biomedical Engineering*, 52(2):306–313, Feb. 2005.

[22] C. Menard, I. C. Smith, R. L. Somorjai, L. Leboldus, R. Patel, C. Littman, S. J. Robertson, and T. Bezabeh. Magnetic resonance spectroscopy of the malignant prostate gland after radiotherapy: a histopathologic study of diagnostic validity. *International Journal of Radiation Oncology Biology Physics*, 50(2):317–323, Jun 2001.

[23] C. K. Naughton, D. C. Miller, D. E. Mager, D. K. Ornstein, and W. J. Catalona. A prospective randomized trial comparing 6 versus 12 prostate biopsy cores: impact on cancer detection. *Journal of Urology*, 164(2):388–392, Aug 2000.

[24] M. Norberg, L. Egevad, L. Holmberg, P. Sparn, B. J. Norln, and C. Busch. The sextant protocol for ultrasound-guided core biopsies of the prostate underestimates the presence of cancer. *Urology*, 50(4):562–566, Oct 1997.

[25] M. J. O'Connell, C. S. Smith, P. E. Fitzpatrick, C. O. Keane, J. M. Fitzpatrick, M. Behan, H. F. Fenlon, and J. G. Murray. Transrectal ultrasound-guided biopsy of the prostate gland: value of 12 versus 6 cores. *Abdominal Imaging*, 29(1):132–136, 2004.

[26] J. C. Presti. Prostate cancer: assessment of risk using digital rectal examination, tumor grade, prostate-specific antigen, and systematic biopsy. *Radiologic Clinics of North America*, 38(1):49–58, Jan 2000.

[27] H. H. Quick, J. M. Serfaty, H. K. Pannu, R. Genadry, C. J. Yeung, and E. Atalar. Endourethral MRI. *Magnetic Resonance in Medicine*, 45(1):138–146, Jan 2001.

[28] F. Rabbani, N. Stroumbakis, B. R. Kava, M. S. Cookson, and W. R. Fair. Incidence and clinical significance of false-negative sextant prostate biopsies. *Journal of Urology*, 159(4):1247–1250, Apr 1998.

[29] K. A. Roehl, J. A. V. Antenor, and W. J. Catalona. Serial biopsy results in prostate cancer screening study. *Journal of Urology*, 167(6):2435–2439, Jun 2002.

[30] D. Stoianovici, D. Song, D. Petrisor, D. Ursu, D. Mazilu, M. Muntener, M. Mutener, M. Schar, and A. Patriciu. MRI stealth robot for prostate interventions. *Minimally Invasive Therapy and Allied Technologies*, 16(4):241–248, 2007.

[31] R. Susil, K. Camphausen, P. Choyke, E. McVeigh, G. G. GS, H. Ning, R. Miller, E. Atalar, C. Coleman, and C. Menard. System for prostate brachytherapy and biopsy in a standard 1.5T MRI scanner. *Magnetic Resonance in Medicine*, 52(3):683–7, September 2004.

[32] R. Susil, A. Krieger, J. Derbyshire, A. Tanacs, L. Whitcomb, G. Fichtinger, and E. Atalar. A system for guidance and monitoring of transrectal prostate biopsy in a 1.5 T closed MR scanner. *European Radiology*, 12(9), 2002.

[33] R. C. Susil, A. Krieger, J. A. Derbyshire, A. Tanacs, L. L. Whitcomb, G. Fichtinger, and E. Atalar. System for MR image-guided prostate interventions: Canine study. *Radiology*, 228(3):886–894, September 2003.

[34] K. Tadakuma, L. DeVita, S. Y., and S. Dubowsky. The experimental study of a precision parallel manipulator with binary actuation: With application to MRI cancer treatment. In *Proc. IEEE International Conference on Robotics and Automation ICRA '08*, pages 2503–2508, May 21–May 23, 2008.

[35] M. K. Terris, J. E. McNeal, F. S. Freiha, and T. A. Stamey. Efficacy of transrectal ultrasound-guided seminal vesicle biopsies in the detection of seminal vesicle invasion by prostate cancer. *Journal of Urology*, 149(5):1035–1039, May 1993.

[36] M. K. Terris, E. M. Wallen, and T. A. Stamey. Comparison of mid-lobe versus lateral systematic sextant biopsies in the detection of prostate cancer. *Urologia Internationalis*, 59(4):239–242, 1997.

[37] A. E. Wefer, H. Hricak, D. B. Vigneron, F. V. Coakley, Y. Lu, J. Wefer, U. Mueller-Lisse, P. R. Carroll, and J. Kurhanewicz. Sextant localization of prostate cancer: comparison of sextant biopsy, magnetic resonance imaging and magnetic resonance spectroscopic imaging with step section histology. *Journal of Urology*, 164(2):400–404, Aug 2000.

[38] C.-F. Westin, S. E. Maier, H. Mamata, A. Nabavi, F. A. Jolesz, and R. Kikinis. Processing and visualization for diffusion tensor MRI. *Medical Image Analysis*, 6(2):93–108, Jun 2002.

[39] K. K. Yu and H. Hricak. Imaging prostate cancer. *Radiologic Clinics of North America*, 38(1):59–85, viii, Jan 2000.

[40] S. Zangos, K. Eichler, K. Engelmann, M. Ahmed, S. Dettmer, C. Herzog, W. Pegios, A. Wetter, T. Lehnert, M. G. Mack, and T. J. Vogl. MR-guided transgluteal biopsies with an open low-field system in patients with clinically suspected prostate cancer: technique and preliminary results. *European Radiology*, 15(1):174–182, Jan 2005.

[41] S. Zangos, C. Herzog, K. Eichler, R. Hammerstingl, A. Lukoschek, S. Guthmann, B. Gutmann, U. J. Schoepf, P. Costello, and T. J. Vogl. MR-compatible assistance system for punction in a high-field system: device and feasibility of transgluteal biopsies of the prostate gland. *European Radiology*, 17(4):1118–1124, Apr 2007.